Diffusive wave spectroscopy applied to the spatially resolved deformation of a solid

Marion Erpelding, Axelle Amon, and Jérôme Crassous[*]

Institut de Physique de Rennes, UMR UR1-CNRS 6251, Université de Rennes 1, Campus de Beaulieu, F-35042 Rennes cedex, France

We propose an experimental setup based on diffusive wave spectroscopy for studying deformations of a solid material. The scattered waves are measured during the deformation of the solid material at different locations of its surface. The correlations of the scattered intensities are measured. The loss of correlation can be related to the invariants of the strain tensor of the solid, giving us a spatially resolved determination of the deformation near the surface. Experiments dealing with a point stress on plate for two kinds of elastic materials are presented and compared with the theoretical predictions.

I. INTRODUCTION

Determining the deformations of solid materials under applied stresses is an important issue for many fields of research such as the elastic deformations of a solid body [1], apparition and propagation of failures [2], or the study of plastic behavior of soils [3–5].

Optical methods are classical nondestructive methods for these studies. The deformation of solid surfaces may be directly measured by recording with a camera different points on the solid surfaces and analyzing their displacements using techniques borrowed from fluid mechanics studies such as particle image velocimetry [6] or digital image correlations [7]. Speckle measurements use the random interference patterns of coherent light reflected by the surface and measure their displacements with different interferometric techniques [8].

In the displacement measurements mentioned above, the light does not penetrate through the samples. The goal of this paper is to propose an extension of these methods to the case where the light interacts strongly with the material and penetrates through the sample.

As a consequence of the interaction between light and the material, a scattering of light takes place. The study of the temporal variation of the scattered electric field or intensity may be used to get information about the dynamics of scattering media [9]. Those techniques are routinely used to characterize the random motion of colloidal particles, foam dynamics, or the dynamics of gelating processes [9,10]. The application of light scattering techniques in highly diffusing materials for studying the shear flow of a turbid fluid has been proposed and demonstrated [11–14]. In these experiments, the loss of the correlation of the scattered light comes from the shearing flow of the scatterers, to which is added a random Brownian motion of the scatterers.

In this paper, we analyzed the light scattered by an optically diffusing solid material after it penetrates through the sample and used it to measure the heterogeneous deformation of this sample subject to stress. For this, we developed a light scattering setup to measure the speckle pattern of the light backscattered from a solid surface lightened by a planar wave. Light emerging from a point of the surface has explored a volume within the solid which is determined by the optical properties of the material. This defines the spatial resolution of the method. In order to study nonstationary deformations of the body, we used a multispeckle scheme [15]. The relation between the loss of correlation of the scattered light and the deformation of the body is derived from theoretical considerations on light propagation through a random medium.

We begin this paper in Sec. II with a theoretical background where we recall some general considerations on diffusive wave spectroscopy. The relation between the intensity correlations and the variation of photon path lengths are recalled. The relation between the length variations and the strain tensor are then explained. In Sec. III we explain how to design the experimental setup in order to have a spatially resolved measurement of the deformation. In Sec. IV, we introduce the experimental setup consisting of two different elastic materials submitted to a variable point load. In Sec. V we present the experimental maps of light intensity correlation when the force is increased and decreased. In Sec. VI we compare these maps with the ones expected from linear elasticity. We first compare the results with a simple analytical expression for the correlation of the scattered intensity in Sec. VI A, and then with a numerical simulation of deformed photon paths in Sec. VI B. We finish with concluding remarks in Sec. VII.

II. THEORETICAL BACKGROUND

In a dynamical light scattering experiment, a scattering medium is illuminated by a coherent light field and the fluctuations of the collected scattered light are used to analyze the dynamics of the scattering medium [9]. Because of the random structure of the medium, the scattered light shows a speckle spatial structure defining areas of coherence in the scattered field. Typically, the total intensity of one coherence area is collected for two different states 1 and 2 of the scattering medium, giving two intensities I_1 and I_2. Information on the displacements in the scattering medium can be deduced statistically from the correlations between those two intensities, through the calculation of the autocorrelation function $\langle I_1 I_2 \rangle$ on a statistical ensemble, where $\langle \cdots \rangle$ represents a temporal or ensemble average. When the dynamical

*jerome.crassous@univ-rennes1.fr

system is stationary, a temporal average is used to calculate autocorrelation functions, yet, such a method cannot deal with slow dynamics and nonstationary systems. Otherwise, a statistical average can be achieved by simultaneously collecting intensities from several coherence areas forming a statistical ensemble of independent intensities [15].

When the scattered field is Gaussian distributed, the intensity autocorrelation function is linked to the normalized electric field autocorrelation function between electric fields scattered in two different states 1 and 2,

$$g_E^{(12)} = \frac{\langle E_1 E_2^* \rangle}{\langle |E_1| \rangle \langle |E_2| \rangle} \qquad (1)$$

via the Siegert relation [9]

$$\frac{\langle I_1 I_2 \rangle}{\langle I_1 \rangle \langle I_2 \rangle} = 1 + \beta_e |g_E(1,2)|^2, \qquad (2)$$

where β_e is an experimental constant of order unity depending on the details of the experimental setup [9].

For highly diffusive materials, a photon propagating inside the sample follows a random walk which may be described in the diffusion approximation [16–18]. In this framework, the correlation function of the scattered field may be expressed as [10,16]

$$g_E^{(12)} = \int_s P(s) \langle \exp^{j\Delta\phi_s(1,2)} \rangle ds, \qquad (3)$$

where $\Delta\phi_s(1,2)$ is the phase difference of an optical path of length s between the states 1 and 2 and contains the information about the motion of the scatterers. $\langle \cdots \rangle$ is an average over all paths of length s. $P(s)$ is the path length distribution, and depends on the optical properties of the materials and on the geometry of the experiment [18].

An example of deformation of an optical path between two different states 1 and 2 is schematically represented in Fig. 1(a) in a backscattering configuration.

For a scattering medium which is being deformed, the phase variation for a path $\phi(1,2) = \phi(2) - \phi(1)$ between the two states 1 and 2 is linked to the displacement field $\mathbf{u}(\mathbf{r})$. We define in Fig. 1(b) a discretized description of a path: If ν indexes the number of the scattering event among the N events forming the path, each event takes place at a position $\mathbf{r}_\nu^{(i)}$ for state i. The displacement field is then defined as $\mathbf{u}_\nu = \mathbf{r}_\nu^{(2)} - \mathbf{r}_\nu^{(1)}$. The phase variation for a given path is then

$$\Delta\phi = \sum_{\nu=0}^{N} k l_\nu \mathbf{e}_\nu \cdot (\mathbf{e}_\nu \cdot \boldsymbol{\nabla}) \mathbf{u}(\mathbf{r}_\nu), \qquad (4)$$

where k is the wave vector of the light field: $k = 2\pi/\lambda$ with λ the wavelength of light in the medium, $l_\nu = \|\mathbf{r}_{\nu+1} - \mathbf{r}_\nu\|$ is the distance between two successive scattering events ν and $\nu+1$ along the direction $\mathbf{e}_\nu = (\mathbf{r}_{\nu+1} - \mathbf{r}_\nu)/l_\nu$ [see Fig. 1(b)].

The diffusion of light length scale l is given by the average $\langle l_\nu \rangle$. When the displacement field varies slowly at the length scale l [11,13], we can expand (4) to first order
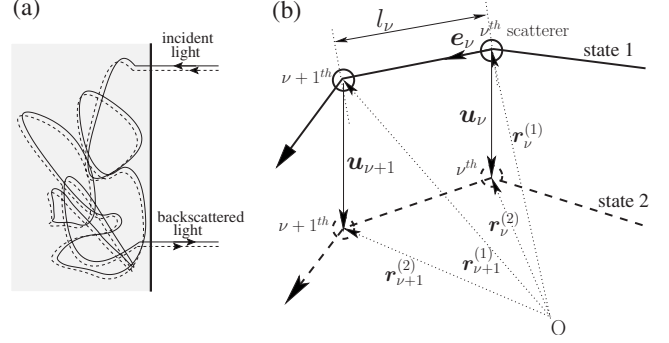
FIG. 1. (a) Schematic of a multiple dynamic light scattering experiment in a backscattering configuration. The solid line represents an example of a path followed by a ray in the first state of the scattering medium, the dashed line shows how this path has been modified in state 2. (b) Discretized representation of the diffusion in the medium: Circles represent the νth and $\nu+1$th scatterers for states 1 (solid line) and 2 (dashed line). Vectors $\mathbf{r}_\nu^{(i)}$ give the position of the νth scatterer in state i. The displacement field is given by $\mathbf{u}_\nu = \mathbf{r}_\nu^{(2)} - \mathbf{r}_\nu^{(1)}$.

$$\Delta\phi = k \sum_{\nu=0}^{N} l_\nu \sum_{i,j} e_{\nu,i} e_{\nu,j} U_{ij}(\mathbf{r}_\nu), \qquad (5)$$

where $\mathbf{U}$ is the strain tensor of components $U_{ij} = (1/2)(\partial u_i / \partial j + \partial u_j / \partial i)$, and i and j designate Cartesian coordinates.

In the multiple scattering limit, the number of events N implied in a random path is large and by the central limit theorem $\Delta\phi$ is a random Gaussian variable. Consequently, when averaging over all the possible paths with the same number of scattering events N, hence of same length $s = Nl$,

$$\langle \exp(i\Delta\phi_s) \rangle = \exp(i\langle \Delta\phi_s \rangle) \exp\left(-\frac{\langle \Delta\phi_s^2 \rangle - \langle \Delta\phi_s \rangle^2}{2} \right). \quad (6)$$

The mean value and the variance of the phase fluctuations may then be related to the components of the strain tensor U_{ij} along paths. Moreover, when the light is multiply scattered, the orientation of the different directions of scattering are isotropic, and $\langle \Delta\phi_s \rangle$ and $\langle \Delta\phi_s^2 \rangle$ can be expressed as functions of the isotropic invariants of the strain tensor. If there is no correlation between the lengths l_ν and the orientations $\mathbf{e}_\nu$, averages are independent, and the first moment is then [11,13]

$$\langle \Delta\phi_s \rangle = \tfrac{1}{3} k s \, \mathrm{Tr}(\mathbf{U}), \qquad (7)$$

where $\mathrm{Tr}(\mathbf{U}) = \Sigma_i U_{ii}$ and where we used $\langle e_{\nu,i} e_{\nu,j} \rangle = \delta_{ij}/3$.

The general expression of the second moment is

$$\langle \Delta\phi_s^2 \rangle = k^2 \sum_{\nu,\nu'} \langle l_\nu l_{\nu'} \rangle \sum_{ij,i'j'} \langle e_{\nu,i} e_{\nu,j} e_{\nu',i'} e_{\nu',j'} \rangle \langle U_{ij} U_{i'j'} \rangle. \qquad (8)$$

Further simplifications of (8) require some knowledge of the path of photons through the solid medium. However, the quadratic dependence on U_{ij} combined with the isotropic orientation of scattered rays leads to a dependence of the vari-

ance on the two quadratic isotropic invariants of the strain tensor $\mathrm{Tr}^2(\mathbf{U})$ and $\mathrm{Tr}(\mathbf{U}^2) = \Sigma_{i,j} U_{ij}^2$. Besides, the phase shift is the sum of a large number of independent events. Consequently, its variance is linear with the number of events N and then with the path length s. Those considerations lead to [19]

$$\langle \Delta \phi_s^2 \rangle - \langle \Delta \phi_s \rangle^2 = k^2 s [(\beta - \chi) \mathrm{Tr}^2(\mathbf{U}) + 2\beta \mathrm{Tr}(\mathbf{U}^2)], \quad (9)$$

where β and χ are constants which have the dimension of length. These values depend on the details of the light propagation through the material. They may be calculated for a medium consisting of Mie scatterers dispersed in a homogeneous matrix. In this case, Bicout et $al.$ have shown that $\beta = 2l^*/15$ and $\chi = 0$ [11,13]. In the former expression, the transport mean free path l^* has been introduced. It is the distance over which the direction of light propagation is randomized and differs from l, the mean length between two scattering events, because of the local anisotropy of the scattered field [18].

The determination of $g_E^{(1,2)}$ may be obtained from Eq. (3). For this, the path length distribution $P(s)$ must be known. This quantity depends on the experimental illumination and detection geometry. It may be computed from the diffusion equation with the boundary conditions corresponding to the geometry of the experiment. Analytical expressions of the integrals (3) are computed in the case of light diffusion in a medium composed of independently moving scatterers (suspension of colloidal particles). In this case [10,16]

$$\langle \Delta \phi_s^2 \rangle - \langle \Delta \phi_s \rangle^2 = k^2 s \frac{2}{3} \frac{\langle \Delta r^2 \rangle}{l^*}, \quad (10)$$

where $\langle \Delta r^2 \rangle$ is the mean quadratic displacement of scatterers. Expression (9) may be linked to (10) with the formal substitution

$$(\beta - \chi) \mathrm{Tr}^2(\mathbf{U}) + 2\beta \, \mathrm{Tr}(\mathbf{U}^2) \leftrightarrow \frac{2}{3} \frac{\langle \Delta r^2 \rangle}{l^*}. \quad (11)$$

In the case of a backscattering geometry where the sample is illuminated by a plane wave and with a point detection [20]

$$|g_E^{(12)}| \approx \exp[- \eta k l^* \sqrt{3 f(\mathbf{U})}], \quad (12)$$

where we have introduced for the sake of simplicity

$$f(\mathbf{U}) = \frac{\beta - \chi}{2l^*} \mathrm{Tr}^2(\mathbf{U}) + \frac{\beta}{l^*} \mathrm{Tr}(\mathbf{U}^2). \quad (13)$$

In (12), η is a numerical factor of order unity ranging from 1.5 to 2.7 and depending on the polarization states of the illuminating and the scattered light [10,21].

Expression (12) for the correlation function of the scattered electric field has been obtained with the assumption that the deformation is homogeneous inside the material. When this is no longer true, the deformation must be weighted by the photon density within the sample [12]. The spatial resolution at which an heterogeneous deformation may be imaged is then dependent on the photon density within the sample. The resolution is then expected to depend on the illumination and detection geometry. In the following,

we will use the backscattering geometry. For a collimated beam impacting a semi-infinite medium, the spatial repartition of the backscattered light may be obtained from radiative transfer theory [22,23]. The backscattering intensity is peaked around the collimated source with an extension of order $\sim l^*$. More precisely, assuming that a diffusing light transport is fully valid, one-half the photons emerge at a distance less than $2.7l^*$ from the center of the beam. Reciprocally, one-half the photons collected at a given point of the surface have been sent at a distance less than $2.7l^*$ from the collecting point. This indicates that in a backscattering geometry, the expected resolution is of the order of a few l^*. However, there are also photons propagating along paths of length $\gg l^*$ through the sample that will not probe the deformation locally. Thus, Eq. (12) is only expected to hold at a precision level depending on the amount of photons which explore the sample nonlocally. For a spatial resolution of order a few l^*, we then expect that (12) should be not able to measure magnitude of deformation with more than a factor ~ 2 in precision. We did not try to quantify analytically these effects in this paper. However, in Sec. VI, we will not only compare Sec. VI A the experimental results with expression (12), but also with the results of a numerical simulation of photon paths which are deformed into a heterogeneous strain field Sec. VI B.

III. PRINCIPLE OF THE MEASUREMENT

We designed the experimental setup in order to obtain the characteristic function $f(\mathbf{U})$ of the deformation field for a body with an inhomogeneous deformation field. We use a backscattering geometry: The front face of our sample is conjugated with a lens on the matrix of a CCD camera. The obtained image is divided into several zones, each of which containing enough coherence areas in order to calculate an average of the intensity autocorrelation functions for the zone. A map of the field autocorrelation function can be deduced and compared to theoretical elasticity calculus using Eqs. (12) and (13).

The optical setup is chosen to take several constraints into account. To begin with, several lengths are fixed in our setup by our equipment: The wavelength of the laser λ, the size of one pixel l_p and the size of the CCD matrix $n_p l_p$, with n_p the number of pixels in a row, and finally, the transport mean free length of the medium l^*.

Two parameters are estimated to obtain optimal use of all the pixels of the CCD camera. First, one coherence area must cover several pixels of the camera but each pixel of the same coherence area will contain the same information. The minimal size expressed in number of pixels for a speckle has been determined by Viasnoff et $al.$ [15]: $n_c \simeq 3$, then the typical size of a coherence area on the camera should be

$$l_c = n_c l_p. \quad (14)$$

Second, as explained previously, a photon will explore a volume of typical size l^* in its random walk before leaving the medium. The information is thus naturally averaged over a volume of $(l^*)^3$, as shown in Fig. 2(a). Consequently, the transport mean free length l^* determines the maximal experi-
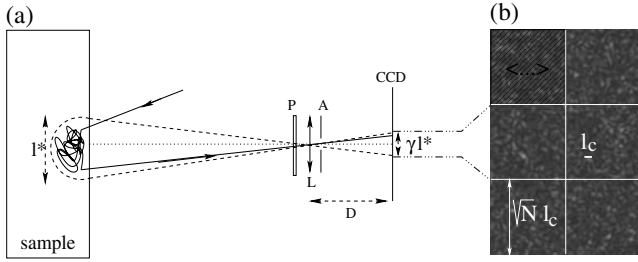
FIG. 2. (a) Schematic of the optical imaging device. An example of a ray path is shown as the solid line. P is a polarizer, L is the lens, and A is the diaphragm aperture. (b) Example of a part of a speckle image obtained on the CCD in a case where $n_c > 3$. A coherence area has a typical size l_c. Ensemble averages are done over N_c speckles and consequently on areas of size $\sqrt{N_c} l_c$: Each square gives a unique final metapixel. The optical setup (a) is chosen so that $\gamma_t l^* = \sqrt{N_c} l_c$.

mental resolution attainable. With a transversal lens magnification of γ_t, the size of the corresponding area on the image is $\gamma_t l^*$ and determines the domain in which the ensemble average over several coherence areas should be done [one square on Fig. 2(b)]. If N_c is the number of coherence areas over which ensemble averages are performed, we have

$$\gamma_t l^* = \sqrt{N_c} l_c, \quad (15)$$

where N_c is chosen large enough to obtain a respectable ensemble average. As it has already been supposed that the displacement field varies slowly on the length scale l^*, it can be considered as a constant for the natural averaging over a volume $(l^*)^3$. Consequently, for each area corresponding to one metapixel, the deformation can be considered homogeneous and Eq. (12) locally holds. The size of the object is $l_o = n_p l_p / \gamma_t = n_p l^* / (\sqrt{N_c} n_c)$. Increasing l_o would diminish γ_t and N_c so that the ensemble for the average would be smaller. The number of pixels in the final image, called metapixels in the following and corresponding to one square on Fig. 2(b), is $N_c (n_p / n_c)^2$.

There is only one adjustable parameter left: The diameter of the aperture of the diaphragm d or the distance D between the diaphragm and the camera, the two of which being linked by $d/D = \lambda / l_c$.

We may notice that when the material is submitted to stress, there is also a rigid displacement of the scattering surface. This will produce a displacement of the speckle pattern on the camera sensor, and this displacement may also change the level of correlation of the scattered intensity. This effect is expected to occur when the displacement of the speckle pattern is of order $\sim l_c$ on the camera sensor. This corresponds to a displacement $\sim l_c / \gamma_t$ of the scattering surface in the plane of observation. We will see in the next section that $l_c / \gamma_t \sim 50 \ \mu$m for our experimental setup. In the following, the actual displacement of the surface is always at least two orders of magnitude smaller. This makes the change of correlation due to the shift of surfaces negligible with respect to the change due to the bulk deformation of the sample.

IV. EXPERIMENTAL SETUP

We used two different kinds of elastic, light-scattering materials. The first one is a dispersion of latex spheres in a gelatine matrix. For this, we prepared an aqueous solution of gelatin (Vahiné) with a mass fraction of 7% of gelatine. Latex spheres of diameter $d = 1.09 \ \mu$m from Sigma-Aldrich at a 0.5% volume fraction are then dispersed in the aqueous solution. A $(25 \times 15 \times 10)$ mm^3 block of gel is molded and left to gel for a few hours at ambient temperature. An observation of the sample under the microscope shows that the latex spheres are well dispersed in the gel and do not form any clusters. The Young's modulus of the gelatine block has been measured $E = 5.5 \pm 1.5$ kPa. The second scattering material considered is Teflon (polytetrafluoroethylene, PTFE, tabulated Young's Modulus $E = 500$ MPa). We used a slab of Teflon of 4 cm $\times$ 3 cm for a thickness of 5 mm. We will consider that the two materials are incompressible (Poisson's ratio $\nu \simeq 0.5$). The optical scattering properties of the two materials are measured by comparing the transmitted intensity T of slabs to the transmission of a calibrated dispersion of latex spheres. The transmission as a function of the thickness, $T(L)$, depends on two parameters: The absorption length L_a and the mean free length l^* [24]. For $l^* \ll L_a$, keeping notations of Ref. [24],

$$T(L) \simeq (\gamma_T + \beta_T) \frac{l^*}{L_a} \frac{1}{\sinh(L/L_a)} \simeq \frac{5}{3} \frac{l^*}{L_a} \frac{1}{\sinh(L/L_a)}, \quad (16)$$

where $\gamma_T \simeq 1$ and $\beta_T \simeq 2/3$ are two transport parameters which are defined in [24]. By fitting this function to the experimental data at different thicknesses, we obtained the mean free length. For gelatine we found $l^* = 435 \ \mu$m, which is close to the expected value $l^* = 500 \ \mu$m for an aqueous solution of latex spheres of the same concentration. This is in agreement with the fact that the gel is mainly composed of water, and the scattering properties of a latex sphere embedded in gelatin should be close to those of the same sphere in water. For Teflon, we found $l^* \simeq 260 \ \mu$m.

The experimental setup is shown in Fig. 3. We use a Ventus continuous-wave linearly polarized laser of wavelength 532 nm and maximal power ~ 50 mW. The beam emerging from the laser source is expended by a microscope objective (M in Fig. 3) of magnification $\times 10$. The beam incident on the sample is sufficiently wide so that the intensity is roughly spatially homogeneous on the imaged surface. Averaging per zone smooths out the remaining inhomogeneities of the transverse profile. The camera is a DALSA PT-41-04M60 of 2352×1728 resolution and pixel size 7.4 μm.

The choice of the value of N_c is a compromise for the quality of the final image between the final resolution ($\propto 1/N_c$) and the signal-to-noise ratio of a single zone ($\propto \sqrt{N_c}$). A value of $N_c \simeq 180$ coherence areas gives 58 $\times 43$ metapixels for the final image, corresponding to an object of size 3.6 cm $\times$ 2.6 cm. An example of an obtained image is shown in Fig. 3. The magnification of the lens must be $\gamma_t \simeq 0.5$ which is obtained by choosing a focal length $f' = 100$ mm for the lens L and a distance $D = 150$ mm between the lens L and the CCD of the camera. The diaphragm aperture has then a diameter $d \simeq 3.6$ mm. The polarizer P allows
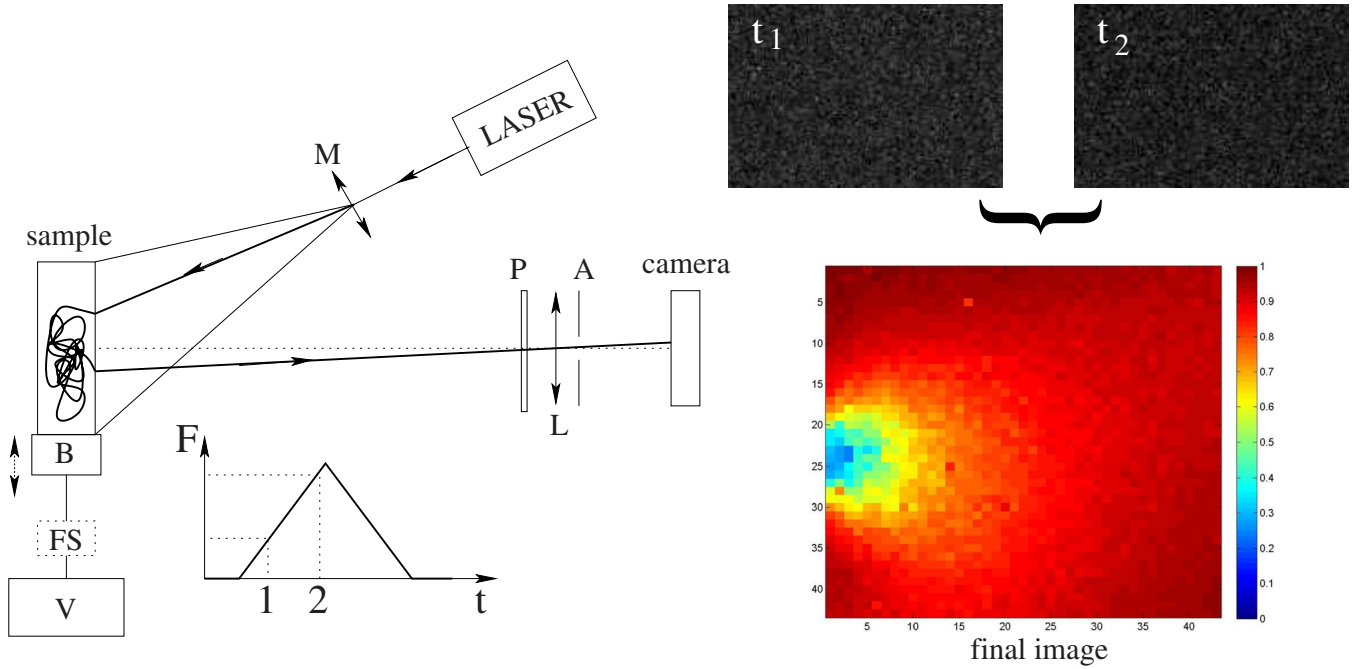
FIG. 3. (Color online) Schematic of the experimental setup. M designates the microscope objective, P, L, and A are the same as on Fig. 2. The periodic displacement of a blade B thanks to a vibrator V exerts a force F on a side of the slab. The applied force is measured with a force sensor FS. Parts of images taken by the camera at two different times corresponding to two different forces are shown. Under them is the resulting calculation of the spatially resolved intensity correlation function.

us to collect one direction of polarization in the depolarized scattered light.

To illustrate the principle of the measurement we consider the deformation of an elastic body in a plane stress configuration: A force is exerted normally by a blade on a side of a slab of elastic material. The blade is in contact with the sample side along a line oriented perpendicularly to the observation plane in order to produce a two-dimensional stress field. Actually, even if the stress field is two dimensional in a good approximation, the collected information is not two dimensional. The random walk of the optical rays is three dimensional, of characteristic length extension l^*. To exert a force we use a vibrator (Brüel&Kjær4810). The moving part is a coil wound around a fixed permanent magnet. A ramp of intensity in the coil leads to a normal stress on the slab. For the gelatine sample, the applied force is measured with a force sensor (Futek FSH02665) mounted between the sensor and the blade, and for Teflon, the force is deduced from the current applied to the coil.

Different states of the sample correspond to different values of the force. An example is given in Fig. 3: The two states correspond to two different times during the ramp of the vibrator. Parts of the two images taken by the camera at times t_1 and t_2 are shown, as well as the resulting measured spatially resolved intensity correlation function,

$$G_{I,mes}^{(12)} = \frac{\langle I_1 I_2 \rangle - \langle I_1 \rangle \langle I_2 \rangle}{\sqrt{\langle I_1^2 \rangle - \langle I_1 \rangle^2} \sqrt{\langle I_2^2 \rangle - \langle I_2 \rangle^2}}, \quad (17)$$

where $\langle \cdots \rangle$ designates average over all pixels of one metapixel.

V. EXPERIMENTAL RESULTS

Figure 4 shows the experimental maps of correlation for the two kinds of samples and for different values of the force variation. The label t refers to the Teflon slab and g to the gelatine block. For the two materials, the sequence of applied forces shown in Fig. 4 is the same, but with different magnitudes. We started with a given force in the state 1, and we increased the force to reach the state 2. The map t_2 (respectively g_2) shows the intensity correlation between the two states 1 and 2 for Teflon (respectively, gelatine). The decorrelation is stronger near the point of force application, and decreases with the distance from this point. Moreover, the curves of constant decorrelation are nearly circular and tangent to the application point.

We may refer to the analytical solution of the stress problem corresponding to our experimental configuration. We consider an idealized plane stress situation: The stress is two dimensional, consisting in a point force applied normally to a semi-infinite slab. The strain tensor is

$$\mathbf{U} = \frac{F}{e} \frac{2}{\pi} \frac{\nu}{E} \begin{pmatrix} \dfrac{z(x^2/\nu - z^2)}{(x^2+z^2)^2} & 0 & \dfrac{1+\nu}{\nu} \dfrac{xz^2}{(x^2+z^2)^2} \\ 0 & -\dfrac{z}{x^2+z^2} & 0 \\ \dfrac{1+\nu}{\nu} \dfrac{xz^2}{(x^2+z^2)^2} & 0 & -\dfrac{z(x^2-z^2/\nu)}{(x^2+z^2)^2} \end{pmatrix}, \quad (18)$$

where F is the applied force, e the thickness of the slab, E is the Young's modulus of the medium, and ν its Poisson's
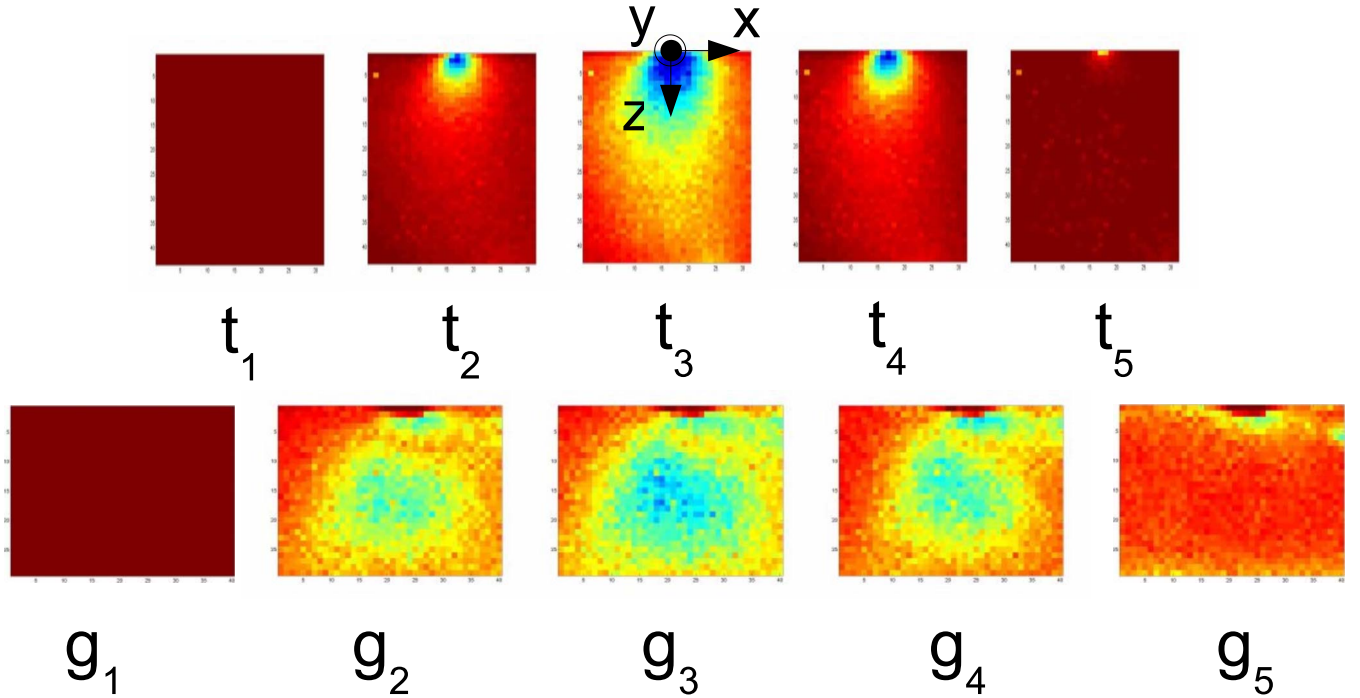
FIG. 4. (Color online) Experimental maps of the intensity correlation function for the two kinds of materials when submitted to an increasing stress followed by a decreasing stress. Maps t_1 to t_5 are for Teflon, and g_1 to g_5 for latex spheres dispersed in gelatine. The change of force between the state 1 and the following states are $F=2.7$ N for (t_2), 8.1 N (t_3), 2.7 N, (t_4), and 0 N (t_5) and $F=0.065$ mN for (t_2), 0.085 mN (t_3), 0.065 mN (t_4), and 0 mN (t_5). The arrows show the axis orientations used for analysis in Sec. VI. Images sizes are 19 $\times$ 27 mm for Teflon, and 14 $\times$ 10 mm for gelatine.

ratio. The force is exerted along the z direction in the xz plane. Isostress solutions are circles all tangent to the point of force application [25]. It follows from (12) and (13) that curves of the same correlation level are also expected to be circles tangent to the point of force application, as is indeed observed.

The force is then increased again in state 3 and the maps t_3 (respectively, g_3) show the intensity correlation between the two states 1 and 3 for Teflon (respectively, gelatine). The nature and the orientation of the curves of constant correlation remain the same, but their magnitude increases. In state 4, the force returned to its value in state 2. The maps t_4 and g_4 show the correlations between the states 1 and 4 and these maps are very similar to the maps t_2 and g_2. This indicates a reversibility of the imposed deformation. When in state 5 the force is at the same level as in state 1, a recorrelation of the scattered intensity occurs. It should be noted that the amount of correlation after such a force cycle differs between Teflon and gelatine samples. While the mean correlation level is $G_{I,mes} \simeq 0.99$ for Teflon, it is $G_{I,mes} \simeq 0.78$ for gelatine. This correlation level is also measured in experiments where no stresses are applied to the gelatine and may then be attributed to the intrinsic dynamics of the material. Some heterogeneities of the decorrelation are also present. Since their localizations vary with the experiment, they may be attributed to imperfections in the preparation of the gelatine sample which are not controlled. It has been checked experimentally that the maps of correlation between two states are not sensitive to the values of the applied force in each state, but only depend on the difference of force between the two states.

VI. ANALYSIS OF RESULTS

A. Theoretical analysis

Previous results can be compared to an analytical expression obtained from the theoretical considerations of Sec. II and from the expression of the strain tensor of the preceding section. Deformations are considered incompressible and $\mathrm{Tr}(\mathbf{U})$ may be neglected in Eq. (13). After some algebraic manipulations, we obtain from Eqs. (13) and (18),

$$f(\mathbf{U}) = \frac{\beta}{l^*}\left(\frac{2F}{e\pi E}\right)^2 (1+2\nu^2)\frac{z^2}{(x^2+z^2)^2}. \quad (19)$$

For the backscattering geometry, Eqs. (12) and (19) lead to
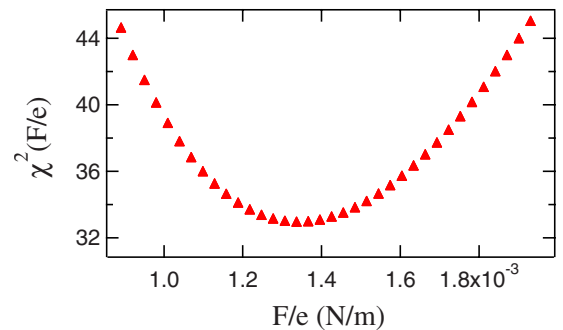
FIG. 5. (Color online) Plot of $\chi^2(\frac{F}{e})$ as defined by (21) as a function of $\frac{F}{e}$.
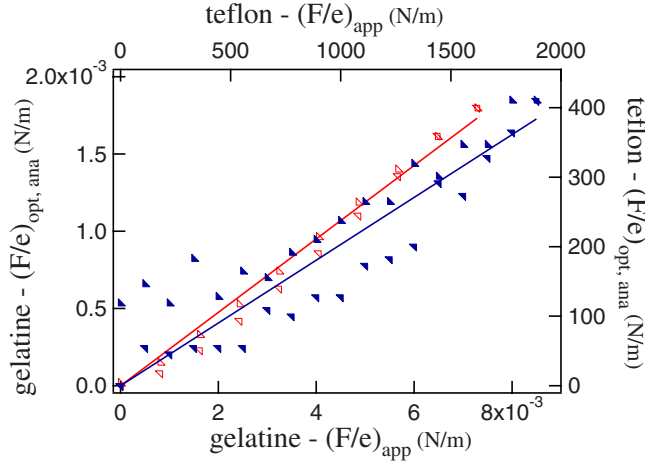
FIG. 6. (Color online) Symbols: $(\frac{F}{e})_{opt,ana}$ as a function of the applied force per unit length $(\frac{F}{e})_{app}$ for the two materials. The force varies from 0 to ≈ 8 N for Teflon (open symbols, top and right-hand axis) and from 0 to ≈ 85 μN for gelatin (filled symbols, bottom and left-hand axis). $(\frac{F}{e})_{opt,ana}$ is determined by the best-fit procedure described in the text. The charge (left-hand triangle) and the discharge (right-hand triangle) are plotted. Affine fits of the experimental values for each material are plotted. The slopes of the fits are 0.24 for Teflon and 0.20 for gelatine.

$$G_I^{(12)} = \exp\left(-\frac{F}{e} 4\eta k \sqrt{\beta l^*} \frac{\sqrt{3(1+2\nu^2)}}{\pi E} \frac{z}{x^2+z^2}\right). \quad (20)$$

In this expression, the experimental variable for a given material is the force F. The mechanical and optical properties of the material are given in Sec. II. The value of η is known to depend on the polarization of the illuminating and scattered light [16,21]. We did not investigate this dependence, and we set $\eta = 2.0$ as is usually observed in backscattering experiments where polarized light is detected. We use $\beta = 2l^*/15$ as explained in Sec. III.

For every correlation map, we determined the best value of $\frac{F}{e}$ with the following procedure: For different values of $\frac{F}{e}$, we compute the square difference

$$\chi^2\left(\frac{F}{e}\right) = \sum_{x_p,z_p} \left[G_{I,mes}^{(12)}(x_p,z_p) - G_I^{(12)}\left(x_p,z_p,\frac{F}{e}\right)\right]^2 \quad (21)$$

between the measured correlation function and the one expected from (20). In (21) $\sum_{x_p,z_p}$ designates a sum over all the metapixels.

Figure 5 shows a plot of χ^2 as a function of $\frac{F}{e}$ for one correlation map. The value of $\frac{F}{e}$ that minimizes χ^2, called $(\frac{F}{e})_{opt,ana}$ in the following, may be located with a typical relative error of few % for the two materials. Except for the first pixel located near the tip and a few other pixels, the difference $\{G_{I,mes}^{(12)}(x_p,z_p) - G_I^{(12)}[x_p,z_p,(\frac{F}{e})_{opt,ana}]\}^2$ is everywhere smaller than 10^{-3} for Teflon and 10^{-1} for gelatine. For the latter, there is a natural decorrelation with time described in Sec. V.

Figure 6 represents the variation of $(\frac{F}{e})_{opt,ana}$ as a function of $(\frac{F}{e})_{app}$ in experiments where the applied force is increased and then decreased back to its original value, as in Sec. V.

The variation of $(\frac{F}{e})_{app}$ ranges from 0 to 2×10^3 N m^{-1} for Teflon and from 0 and 9×10^{-3} N m^{-1} for gelatine. Because of the huge difference in the order of magnitude of the applied forces, there are two different couples of axes on Fig. 6: Bottom left-hand side for gelatine and top right-hand side for Teflon. For each material, the charge and the discharge are plotted with reverse orientation of the symbols.

The relation between $(\frac{F}{e})_{opt,ana}$ and $(\frac{F}{e})_{app}$ is linear, in agreement with the fact that the deformation is proportional to the applied stress. In other words, for these experiments the two media are indeed elastic. The affine fits shown in Fig. 6 give a mean slope $(\frac{F}{e})_{opt,ana}/(\frac{F}{e})_{app}$ of 0.24 for Teflon and 0.20 for gelatine. This means that we measured a smaller loss of correlation than expected. As discussed in Sec. II, the theoretical model is expected to give the deformation within a factor of ~ 2. Consequently, the model, leading to the simple analytical expression of Eq. (12), indeed gives a good qualitative and quantitative interpretation of the experimental results.

The experimental measures of applied forces and our fitting procedure induce errors that we estimate to be a few percent, and our measures of l^* typically have errors of 10%. Light absorption within the samples is known to increase the correlation compared to the absorptionless case. Absorption indeed causes a shift of the photon path length distribution within the sample to lower values. As a consequence, the loss of correlation for a given motion of the scatterers decreases. However, this effect is expected to be negligible given the measured absorptions. For the same reasons as for absorption, considering a finite medium instead of a semi-infinite one should decrease the expected loss of correlation.

To describe our experiments as realistically as possible, we have performed numerical simulations presented in the following section.

B. Numerical analysis

To obtain a complete description of the experiment, we computed a realistic simulation of the scattering and deformation processes in a finite geometry. The only material we used that can be described numerically is the disperse Mie scatterers in the matrix of gelatin for which we have a microscopic model of light propagation. The rules of Mie diffusion for the orientation distribution of the rays can indeed
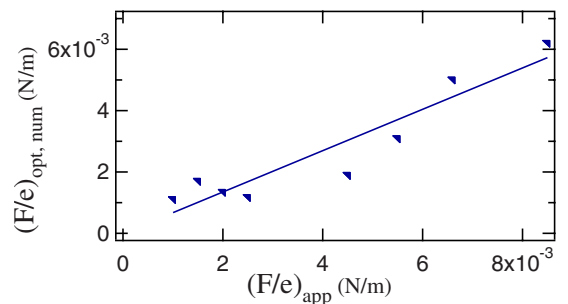
FIG. 7. (Color online) Symbols: $(\frac{F}{e})_{opt,num}$ as a function of the applied force per unit length $(\frac{F}{e})_{app}$. The affine fit giving a slope of 0.67 is plotted.
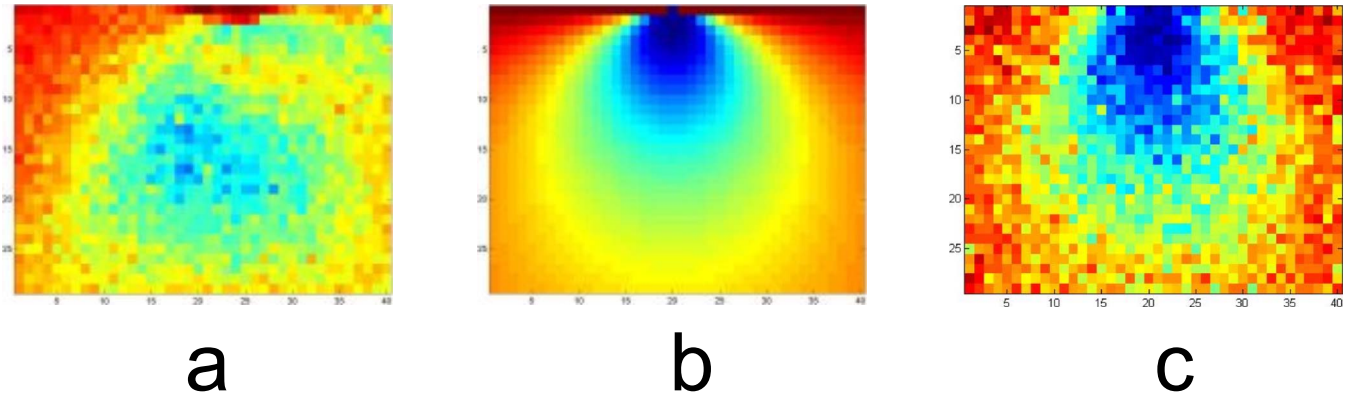
FIG. 8. (Color online) Correlation maps: (a) Experiment, $(\frac{F}{e})_{app}$=0.0085 N/m, (b) analytic calculation, $(\frac{F}{e})_{opt,ana}$=0.0018 N/m, (c) numerical computation, $(\frac{F}{e})_{opt,num}$=0.0062 N/m.

be implemented in the random walk used to describe the photon paths. The distance between the scattering events follows a negative exponential law with a mean distance given by the scattering length. The random walk is performed into a finite parallelepiped of dimension given in Sec. IV. Only backscattered photons are considered in the simulation. For those photons, backscattering paths thus obtained are deformed locally following the Boussinesq displacement field. Phase variations are computed and a numerical correlation function $G_I^{(12)}$ can be calculated for different values of $\frac{F}{e}$.

Using the fitting procedure described in Sec. V A, an optimal value $(\frac{F}{e})_{opt,num}$ can be computed with the same accuracy (i.e., with a relative error of a few percent). Figure 7 represents the variation of $(\frac{F}{e})_{opt,num}$ as a function of $(\frac{F}{e})_{app}$. The affine fit gives a slope $(\frac{F}{e})_{opt,num}/(\frac{F}{e})_{app}$ of 0.67. Consequently, the numerical simulations give a loss of correlation close to the measured one, while the theoretical model given by Eq. (12) tends to overestimate the loss of correlation.

To conclude this section, Fig. 8 shows correlation maps obtained experimentally and by the analyses described previously. Figure 8(a) is the experimental correlation map obtained for $(\frac{F}{e})_{app}$=0.0085 N/m. Figure 8(b) gives the corresponding analytical correlation map calculated with $(\frac{F}{e})_{opt,ana}$=0.0018 N/m and Fig. 8(c) the corresponding numerically computed one with $(\frac{F}{e})_{opt,num}$=0.0062 N/m. The juxtaposition of those three maps clearly demonstrates the accuracy of the method.

VII. CONCLUSION

In this paper we present an experimental method for spatially resolved measurement of deformation of highly scattering solids. We show results obtained with two different scattering materials. To analyze the data, we give a simple analytical expression obtained from theoretical considerations. This model gives a good qualitative and quantitative description of the experiment. Realistic computer simulations allow us to take into account different hypothesis which were neglected in the theoretical model, mainly loss of long length rays because of sample finite size and contribution of long paths experiencing heterogeneous deformation along their length.

In conclusion, the method presented in this paper is an efficient tool for imaging deformations of optically diffusing materials. It gives access to a map of deformation of a layer of thickness a few l^* with a lateral resolution of order of a few l^*. This method is adequate to probe small deformations, in a typical range of strain $\sqrt{\text{Tr}(\mathbf{U}^2)} \sim 10^{-5}-10^{-3}$ for common diffusing materials. Experiments at those scales, which are delicate to address with conventional optical methods, may be applied to the apparition of failure and to the study of the response of soils to stress.

[1] S. P. Timoshenko and J. N. Goodier, *Theory of Elasticity* (McGraw-Hill, Singapore, 1970).

[2] D. François, A. Pineau, and A. Zaoui, *Comportement Mécanique des Matériaux* (Hermes, Paris, 1991).

[3] *Physics of Dry Granular Media*, edited by H. J. Hermann, J-P. Lovi, and S. Luding (Kluwer Academic, Dordrecht, 1998).

[4] R. M. Nedderman, *Static and Kinematics of Granular Materials* (Cambride University Press, Cambridge, 1992).

[5] *Powder and Grains 2005*, edited by R. Garcia-Rojo, H. J. Hermann, and S. MacNamara (Taylor and Francis Group, London, 2005).

[6] R. J. Adrian, Annu. Rev. Fluid Mech. **23**, 261 (1991).

[7] M. A. Sutton, W. J. Wolters, W. H. Peters, W. F. Ranson, and S. R. McNeill, Image Vis. Comput. **1**, 133 (1983).

[8] J. C. Dainty, *Laser Speckle and Related Phenomena* (Springer-Verlag, Berlin, 1989).

[9] B. J. Berne and R. Pecora, *Dynamic Light Scattering With Applications to Chemistery, Biology, and Physics* (Dover, New York, 2000).

[10] *Dynamic Light Scattering: The Method and Some Applications*, edited by W. Brown (Oxford University Press, Oxford, 1993).

[11] D. Bicout, E. Akkermans, and R. Maynard, J. Phys. I **1**, 471 (1991).

[12] D. Bicout and R. Maynard, Physica A **199**, 387 (1993).

[13] D. Bicout and G. Maret, Physica A **210**, 87 (1994).

[14] X. Wu, D. Pine, P. Chaikin, J. Huang, and D. Weitz, J. Opt. Soc. Am. B **7**, 15 (1990).

[15] V. Viasnoff, F. Lequeux, and D. J. Pine, Rev. Sci. Instrum. **73**, 2336 (2002).

[16] D. J. Pine, D. A. Weitz, J. X. Zhu, and E. Herbolzheimer, J. Phys. (France) **51**, 2102 (1990).

[17] G. Maret and P. E. Wolf, Z. Phys. B: Condens. Matter **65**, 409 (1987).

[18] A. Ishimaru, *Wave Propagation and Scattering in Random Media* (Academic, New York, 1978).

[19] J. Crassous, Eur. Phys. J. E **23**, 145 (2007).

[20] L. Djaoui and J. Crassous, Granular Matter **7**, 185 (2005).

[21] F. C. MacKintosh, J. X. Zhu, D. J. Pine, and D. A. Weitz, Phys. Rev. B **40**, 9342 (1989).

[22] R. C. Haskell, L. A. Svaasand, T.-T. Tsay, T.-C. Feng, M. S. MacAdams, and B. J. Tromberg, J. Opt. Soc. Am. A **11**, 2727 (1994).

[23] C. Baravian, F. Caton, J. Dillet, and J. Mougel, Phys. Rev. E **71**, 066603 (2005).

[24] W. Leutz and J. Riča, Opt. Commun. **126**, 260 (1996).

[25] L. Landau and E. Lifchitz, *Théorie de l'élasticité* (Mir, Moscow, 1967).